Electronic Supplementary Material (ESI) for EES Catalysis.
This journal is © The Royal Society of Chemistry 2024

Electronic Supplementary Information

Surface amorphization and functionalization of NiFeOOH electrocatalyst for robust seawater electrolyzer

Hao Wang,[a,c] Nannan Jiang,[a] Bing Huang,[a] Qiangmin Yu[b] and Lunhui Guan*[a]*

[a] State Key Laboratory of Structural Chemistry, Fujian Key Laboratory of Nanomaterials, and CAS Key Laboratory of Design and Assembly of Functional Nanostructures, Fujian Institute of Research on the Structure of Matter, Chinese Academy of Sciences, Fuzhou, Fujian 350002, China.

[b] Shenzhen Geim Graphene Center, Tsinghua-Berkeley Shenzhen Institute & Institute of Materials Research, Tsinghua Shenzhen International Graduate School, Tsinghua University, Shenzhen 518055, P.R. China.

[c] College of Chemistry, Fuzhou University, Fuzhou 350108, China.

Corresponding authors

Qiangmin Yu, e-mail: yu.qiangmin@sz.tsinghua.edu.cn

Lunhui Guan, e-mail: guanlh@fjirsm.ac.cn

Experimental Section

Synthesis of NiFe LDH precursor

First, 3 mmol of $Ni(NO_3)_2 \cdot 6H_2O$ and 1 mmol of $Fe(NO_3)_3 \cdot 9H_2O$ were dissolved in 40 mL of deionized water, 4 mmol of urea and 8 mmol of NH_4F were dissolved in 10 mL of deionized water, then the latter was added dropwise to the former. The solution was then transferred to a round-bottomed flask in an oil bath at 150 ℃ for 6 h. After the reaction, the samples were washed with anhydrous ethanol and deionised water, then dried by freeze dryer.

Synthesis of $Ru_{0.1}$-NiFe LDH

30 mg of NiFe LDH was dispersed in a mixed solvent of anhydrous ethanol and deionised water (the volume ratio of anhydrous ethanol to water was 2:1), and sonicated for 30 min, subsequently. The above solution was pre-stirred for 30 min. Then, the $RuCl_3 \cdot 3H_2O$ (10 wt%) anhydrous ethanol solution was added dropwise to the above solution and stirred for 3 h. The solution was then filtered and washed with isopropanol. The samples were dried in a freeze dryer. The synthesis process of $Ru_{0.01}$-NiFe LDH and $Ru_{0.15}$-NiFe LDH is the same with the $Ru_{0.1}$-NiFe LDH, with the only difference being the amount of $RuCl_3 \cdot 3H_2O$ used, at 1 wt% and 15 wt%, respectively.

Synthesis of $Ru_{0.1}$-NiFeP

0.4 g of sodium hypophosphite and 30 mg $Ru_{0.1}$-NiFe LDH were placed in a glass-porcelain boat, respectively, the former in the upstream of the tube furnace and the latter in the downstream. Subsequently, they were annealed at 400 ℃ (2 ℃/min) for 2 h. The synthesis of NiFeP is the same with $Ru_{0.1}$- NiFeP just without Ru doping process. The synthesis process of $Ru_{0.01}$-NiFeP and $Ru_{0.15}$-NiFeP is the same with the $Ru_{0.1}$-NiFeP.

Preparation of $Ru_{0.1}$-NiFeOOH/PO_4^{3-}

Pre-treatment of the working electrode substrate: First, a piece of nickel foam measuring 1×1 cm^2 is cut. Then, the nickel foam is ultrasonically cleaned in acetone, 1 M HCl, and

deionized water for 15 min each, respectively, to remove any grease and oxidized nickel from the surface of the nickel foam.

Catalyst ink preparation: 5 mg of $Ru_{0.1}$-NiFeP is dispersed in a mixed solvent of 970 μL isopropanol and 30 μL anionic polymer, and sonicated for 2 h to obtain the $Ru_{0.1}$-NiFeP catalyst ink.

The preparation of $Ru_{0.1}$-NiFeOOH/PO_4^{3-} is achieved through the activation of $Ru_{0.1}$-NiFeP via cyclic voltammetry. First, the $Ru_{0.1}$-NiFeP catalyst ink is applied onto pre-treated nickel foam using a pipette, and the loading amount of the $Ru_{0.1}$-NiFeP catalyst is controlled to be 1 mg cm^{-2}. Then, a three-electrode system is utilized, and the activation is carried out for 300 cycles, within the potential range of 0.135-0.235 V vs Ag/AgCl, at a scan rate of 0.1 V s^{-1} vs Ag/AgCl. The preparation method for NiFeOOH/PO_4^{3-} and $Ru_{0.1}$-NiFeOOH is the same, except that $Ru_{0.1}$-NiFeP is replaced with NiFeP and $Ru_{0.1}$-NiFe LDH respectively.

Physical characterization

The structures of samples were first examined by SEM (ZEISS GeminiSEM 300) and TEM (FEI Talos 200S) coupled with energy dispersive X-ray spectroscopy (EDS). The phase information of the electrodes was investigated through X-ray diffraction (XRD) pattern from an MiniFlex 600 with a Cu Kα radiation source. The surface chemical information was measured via X-ray photoelectron spectroscopy (XPS) using an Thermo Scientific K-Alpha system. All measured XPS spectra were calibrated by the C 1s peak (284.8 eV for adventitious hydrocarbon). X-ray absorption structure (XAS) spectra at the Ru K-edges were recorded at the Shanghai Synchrotron Radiation Facility (SSRF). The atomic images of Ru were obtained using a spherical aberration-corrected scanning transmission electron microscope (JEM-ARM300F). Raman spectrum of the electrodes were collected on HORIBA labRAM spectrometer with a 532 nm laser. The elemental composition was determined by ICP-OES (Aglient 5800).

Electrochemical measurements

The electrochemical tests were performed at room temperature on an electrochemical

workstation (CHI 760e). The electrochemical performance was conducted in a standard three-electrode system with different alkaline electrolytes (1 M KOH (PH = 13.8), 1 M KOH + 0.5 M NaCl (PH = 13.8), 1 M KOH + seawater (PH = 13.74), 6 M KOH + seawater (PH = 14.73), detected by PH meter), for which Ag/AgCl/salt bridge and Pt electrodes were used as the reference and counter electrodes, respectively. The catalytic activity including OER and overall water/seawater splitting was collected by reverse linear sweep voltammetry (LSV) curves at a scan rate of 5 mV s^{-1} with 90% IR-correction. The CV curves with scan rates of 20-100 mV s^{-1} were recorded to calculate double-layer capacitance. Electrochemical impedance spectroscopy (EIS) was measured from 100 kHz to 0.01 Hz. All potentials were converted to reversible hydrogen electrode (RHE) through the Nernst equation ($E_{RHE} = E_{Ag/AgCl} + 0.059pH + 0.197$).

Stability measurement: Long-term stability test was carried out in a two-electrode system. Platinum sheet was used as cathode and nickel foam (1×1 cm^2) as anode and the anode loading was 1 mg/cm^2.

Seawater collection: The collection of seawater was done at Xiasha beach, Fujian Province, China. (119°36′ E, 25°47′ N)

Analysis of Hypochlorite by Titration Method

In the analysis of reactive chlorine species, iodide titration was employed. The process began by adjusting the pH of 10 ml of electrolyte to between 1 and 2 using 0.5 M H_2SO_4. Subsequently, 5 mL of 0.5 M KI solution was droped into the mixture while stirring magnetically. Following this, a 0.01 M thiosulfate solution was gradually added. Notably, a yellow coloration emerges in the electrolyte post-thiosulfate addition, indicating the formation of chlorine species.

AEMWE measurement

$Ru_{0.1}$-NiFeOOH/PO_4^{3-} catalyst sprayed on Ni fiber and carbon paper as both anode and cathode (2 cm^2) to assemble anion exchange membrane (AEM) water electrolyzer. An anion

exchange membrane (Sustainion® X37-50-grade T, America) was utilized to separate the cathode and anode. The catalytic performance AEM electrolyzer was measured by a power supply (Interface 5000E, Gamry), While the electrolyte was pumped into electrolyzer with 60 mL min^{-1}. The chronopotentiometry curve of the $Ru_{0.1}$-NiFeOOH/PO_4^{3-} AEM electrolyzer was obtained by recording an average cell voltage at 0.5 A cm^{-2} every 5 s.

DFT calculations

All the DFT computations were carried out using the Vienna ab initio simulation package (VASP). The exchange-correlation energy was evaluated using generalized gradient approximation (GGA) with the Perdew–Burke–Ernzerhof (PBE) functional, and the projector augmented wave (PAW) method was used to describe the electron-ion interactions. The energy cutoff for plane wave expansions was set to 450 eV, and the convergence threshold was set as 10^{-5} eV in energy and 0.02 eV $Å^{-1}$ in force, respectively. For the calculations on the slab models, a vacuum space of 15 Å was added to avoid the interaction between periodic images. In addition, the dipolar correction was adopted for slab models with the symmetrization switching off. K-POINT was set to 2 x 2 x1.

The typical adsorbate evolution mechanism proposed by Nørskov et al. was chosen to evaluate the OER performance for slab models. Briefly, the reaction free energy of each step could be expressed as follows:

$$\Delta G_1 = E(HO*) - E(*) - E_{H2O} + 1/2E_{H2} + (\Delta ZPE - T\Delta S)_1 - eU \quad [1]$$

$$\Delta G_2 = E(O*) - E(HO*) + 1/2E_{H2} + (\Delta ZPE - T\Delta S)_2 - eU \quad [2]$$

$$\Delta G_3 = E(HOO*) - E(O*) - E_{H2O} + 1/2E_{H2} + (\Delta ZPE - T\Delta S)_3 - eU \quad [3]$$

$$\Delta G_4 = E(*) - E(HOO*) + E_{O2} + 1/2E_{H2} + (\Delta ZPE - T\Delta S)_4 - eU \quad [4]$$

where $E(*)$, $E(HO*)$, $E(O*)$, and $E(HOO*)$ are the total energy of the clean surface and the adsorbed surface with three intermediates, respectively. E_{H2O}, E_{H2}, and E_{O2} are the computed energies for the H_2O, H_2, and O_2 molecules, respectively. The values of ΔZPE were determined

by the computed vibrational frequencies and the -eU term represents the external bias U imposed on each step.

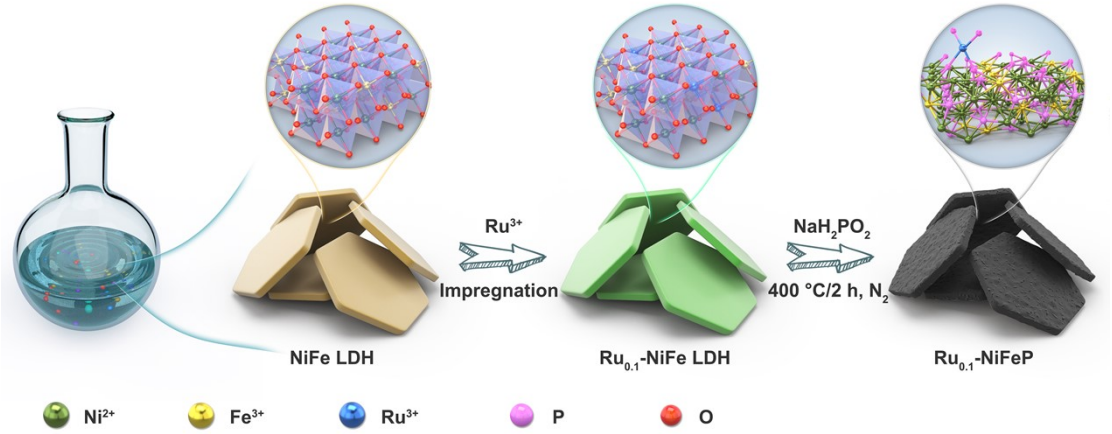

Figure S1 Schematic of the synthesis of pre-catalyst $Ru_{0.1}$-NiFeP.

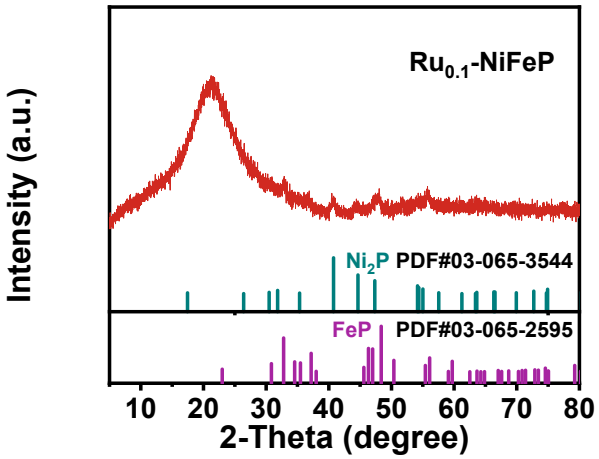

Figure S2 XRD pattern of $Ru_{0.1}$-NiFeP.

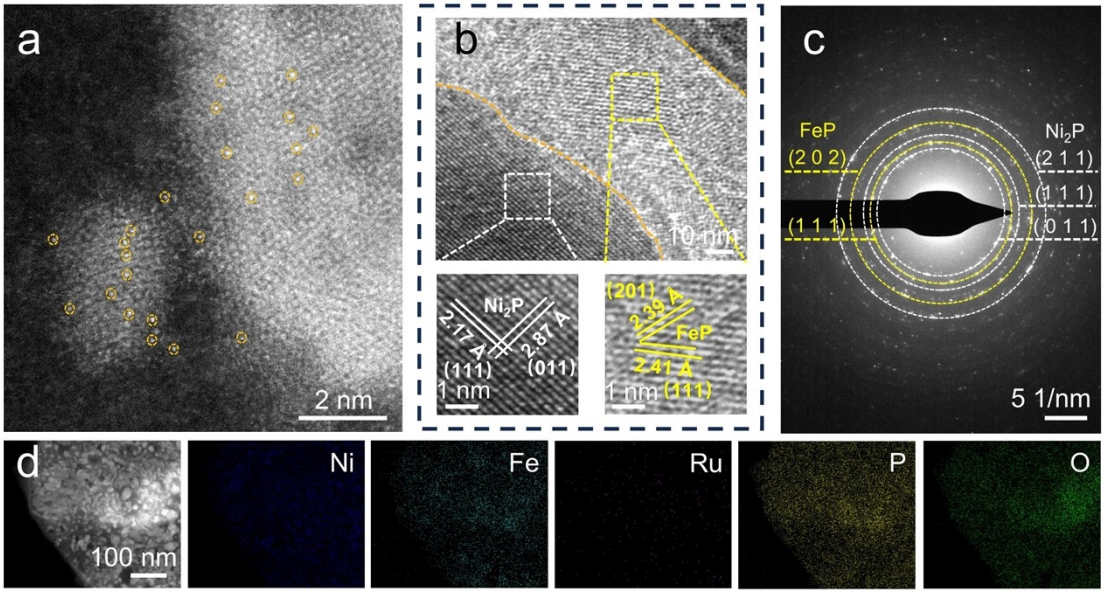

Figure S3 (a) AC-STEM image of $Ru_{0.1}$-NiFeP, (b) HRTEM image of $Ru_{0.1}$-NiFeP and lattice fringes of Ni_2P and FeP, (c) SAED pattern of $Ru_{0.1}$-NiFeP, and (d) HAADF-STEM image and the corresponding elements mapping distribution patterns of $Ru_{0.1}$-NiFeP.

The compositional information of $Ru_{0.1}$-NiFeP is shown in Figure S3. Figure S3a presents the AC-STEM image of $Ru_{0.1}$-NiFeP, where Ru atoms are indicated with yellow markers. It can be observed that in $Ru_{0.1}$-NiFeP, Ru exists in the form of single atoms. Figure S3b displays the HRTEM image of $Ru_{0.1}$-NiFeP; white markers indicate Ni_2P (PDF#03-065-3544), and yellow markers indicate FeP (PDF#03-065-2595). The intact lattice structure of $Ru_{0.1}$-NiFeP, as seen in the image, suggests a high degree of crystallinity. The corresponding SAED pattern (Figure S3c) confirms that $Ru_{0.1}$-NiFeP has a polycrystalline structure. Furthermore, the corresponding elemental mapping images (Figure S3d) reveal a uniform distribution of elements such as Ni, Fe, and Ru throughout $Ru_{0.1}$-NiFeP.

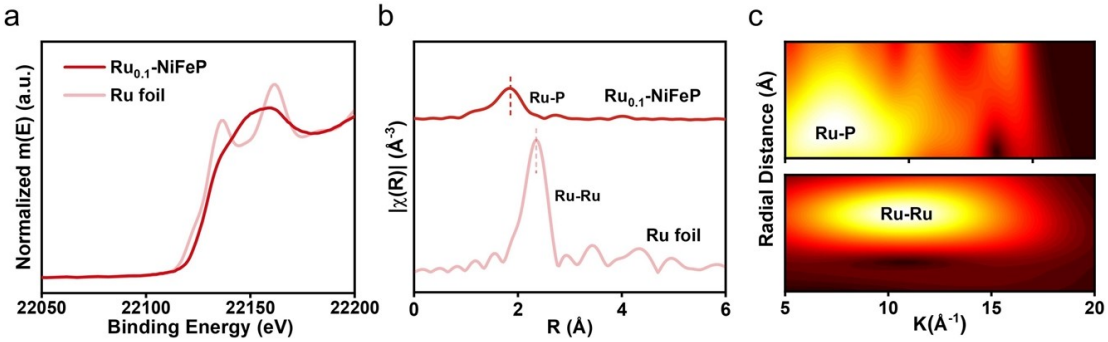

Figure S4 (a) Ru K-edge of $Ru_{0.1}$-NiFeP and Ru foil, (b) k^3 weight Fourier transform spectra from EXAFS of $Ru_{0.1}$-NiFeP and Ru foil, (c) WT-EXAFS plot for $Ru_{0.1}$-NiFeP and Ru foil.

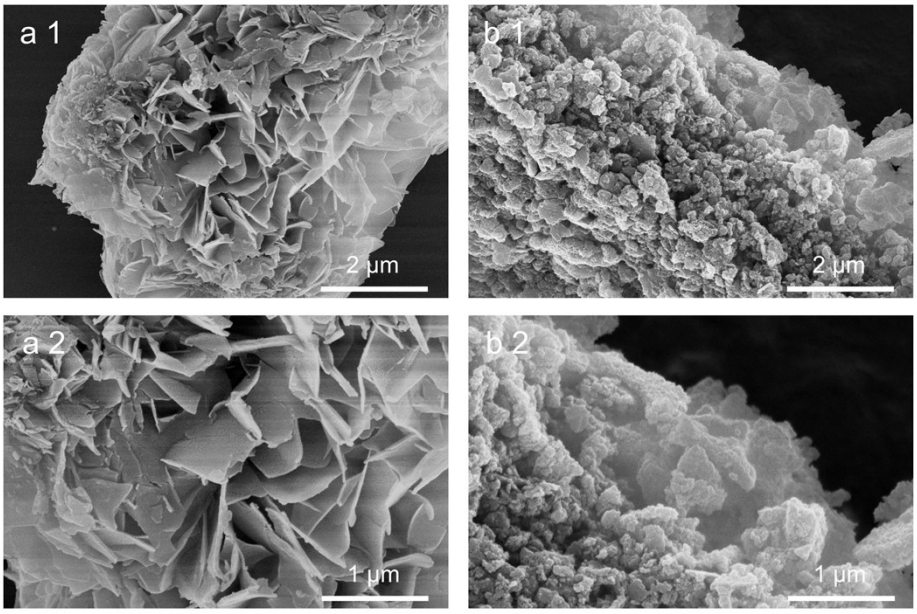

Figure S5 SEM images of (a1-a2) $Ru_{0.1}$-NiFe LDH and (b1-b2) $Ru_{0.1}$-NiFeOOH/PO_4^{3-}.

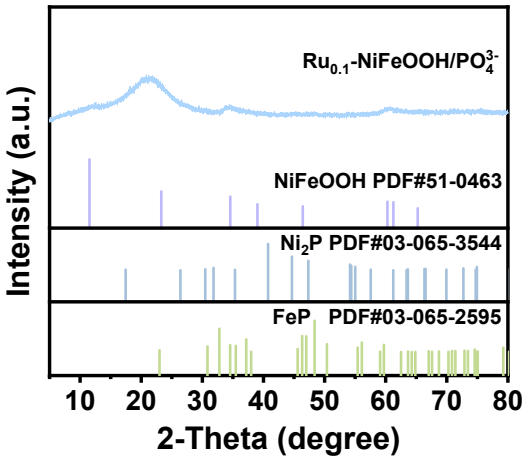

Figure S6 XRD pattern of $Ru_{0.1}$-NiFeOOH/PO_4^{3-}.

Figure S7 (a) HR-TEM and (b) SAED images of $Ru_{0.1}$-NiFe LDH.

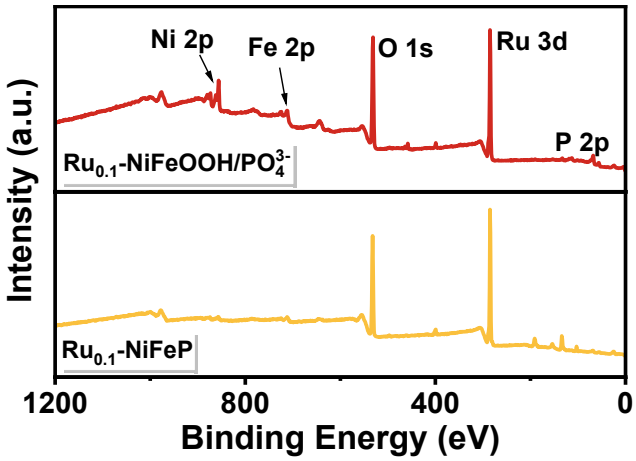

Figure S8 XPS survey of the $Ru_{0.1}$-NiFeOOH/PO_4^{3-} and $Ru_{0.1}$-NiFeP electrocatalysts.

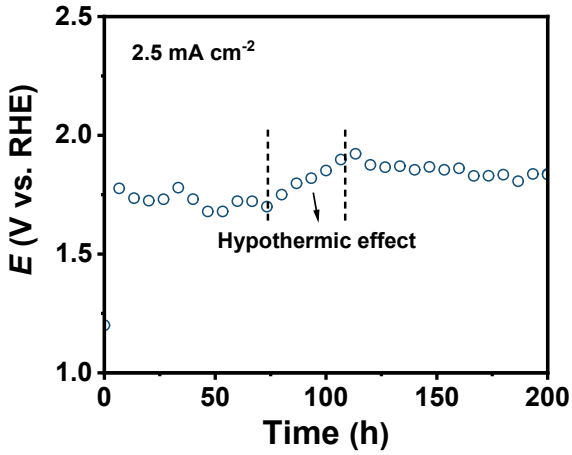

Figure S9 E-T curve for the activation of $Ru_{0.1}$-NiFeOOH/PO_4^{3-}.

To study the surface information of $Ru_{0.1}$-NiFeOOH/PO_4^{3-}, we applied a certain amount of isopropanol ink (binder-free) of $Ru_{0.1}$-NiFeP onto Ti fiber and activated the $Ru_{0.1}$-NiFeP using chronoamperometry test.

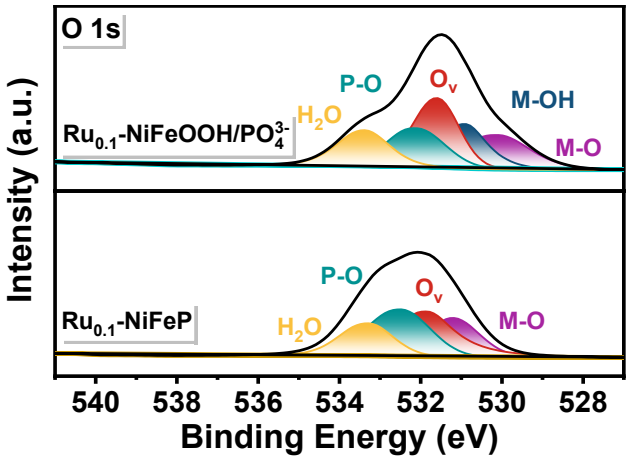

Figure S10 The high-resolution O 1s XPS spectra of $Ru_{0.1}$-NiFeOOH/PO_4^{3-} and $Ru_{0.1}$-NiFeP.

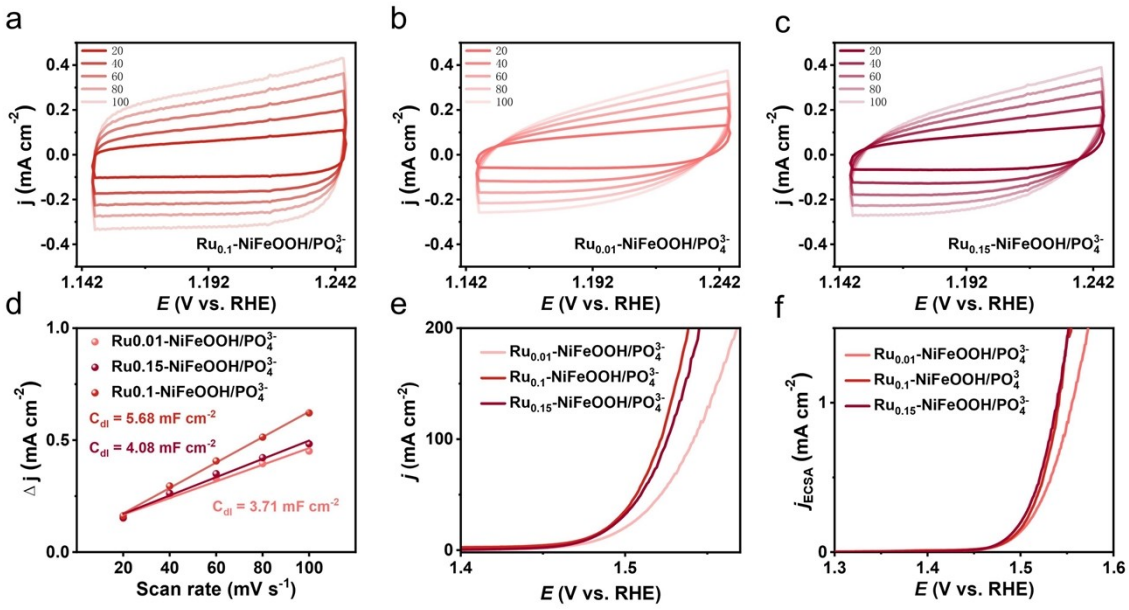

Figure S11 (a-c) CV curves of $Ru_{0.1}$-$NiFeOOH/PO_4^{3-}$, $Ru_{0.01}$-$NiFeOOH/PO_4^{3-}$ and $Ru_{0.15}$-$NiFeOOH/PO_4^{3-}$. (d) Double-layer capacitance (C_{dl}) plots. (e) Polarization curves of samples with different Ru contents. (f) Polarization curves normalized by the corresponding electrochemical active surface area (ECSA) of $Ru_{0.1}$-$NiFeOOH/PO_4^{3-}$, $Ru_{0.01}$-$NiFeOOH/PO_4^{3-}$ and $Ru_{0.15}$-$NiFeOOH/PO_4^{3-}$ electrodes. The ECSA of the catalysts was obtained by ECSA = C_{dl}/C_s, where specific capacitance C_s = 40 μF cm^{-2}.[1]

$ECSA_{Ru0.1\text{-}NiFeOOH/PO43-}$ = 5.68 mF cm^{-2}/40 μF cm^{-2} = 142 cm^{-2}_{ECSA}

$ECSA_{Ru0.01\text{-}NiFeOOH/PO43-}$ = 3.71 mF cm^{-2}/40 μF cm^{-2} = 92.8 cm^{-2}_{ECSA}

$ECSA_{Ru0.15\text{-}NiFeOOH/PO43-}$ = 4.08 mF cm^{-2}/40 μF cm^{-2} = 102 cm^{-2}_{ECSA}

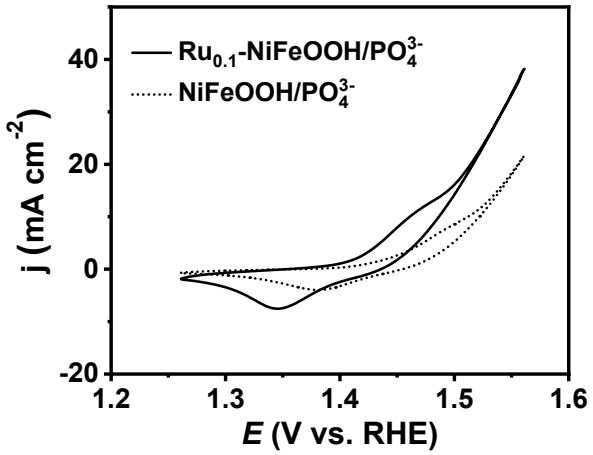

Figure S12 The CV curves of $Ru_{0.1}$-NiFeOOH/PO_4^{3-} and NiFeOOH/PO_4^{3-}.

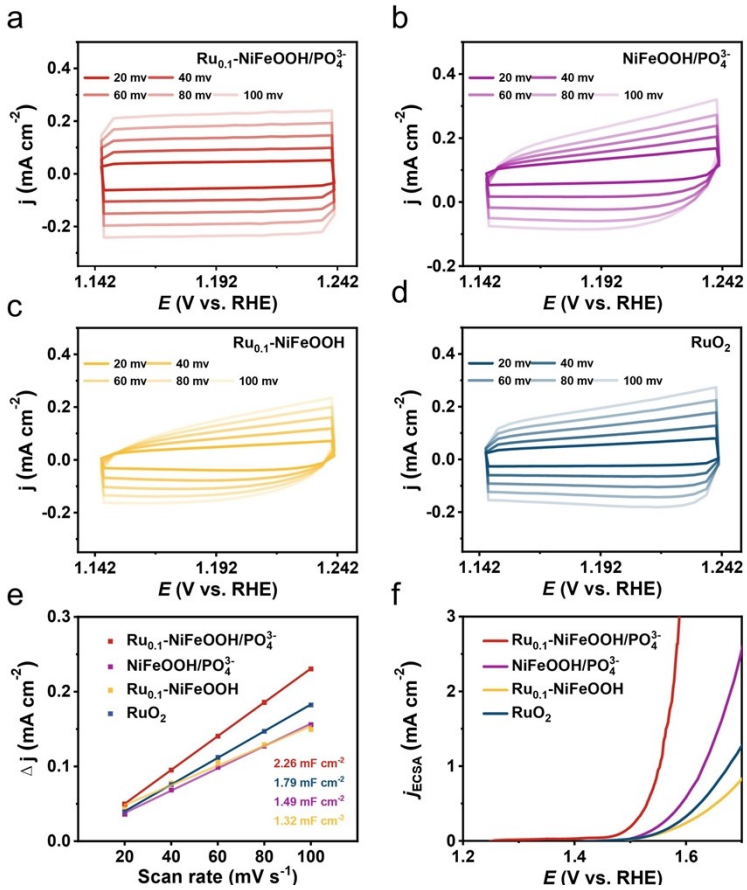

Figure S13 (a-d) CV curves of $Ru_{0.1}$-$NiFeOOH/PO_4^{3-}$, $NiFeOOH/PO_4^{3-}$, $Ru_{0.1}$-NiFeOOH, and RuO_2. (e) C_{dl} plots, and (f) Polarization curves normalized by the corresponding ECSA of $Ru_{0.1}$-$NiFeOOH/PO_4^{3-}$, $NiFeOOH/PO_4^{3-}$, $Ru_{0.1}$-NiFeOOH, and RuO_2 electrodes. The ECSA of the catalysts was obtained by ECSA = C_{dl}/C_s, where specific capacitance C_s = 40 μF cm^{-2}.

$ECSA_{Ru0.1\text{-}NiFeOOH/PO43\text{-}}$ = 2.26 mF cm^{-2}/40 μF cm^{-2} = 56.5 cm^{-2}_{ECSA}

$ECSA_{NiFeOOH/PO43\text{-}}$ = 1.49 mF cm^{-2}/40 μF cm^{-2} = 37.3 cm^{-2}_{ECSA}

$ECSA_{Ru0.1\text{-}NiFeOOH}$ = 1.32 mF cm^{-2}/40 μF cm^{-2} = 33 cm^{-2}_{ECSA}

$ECSA_{RuO2}$ = 1.79 mF cm^{-2}/40 μF cm^{-2} = 44.8 cm^{-2}_{ECSA}

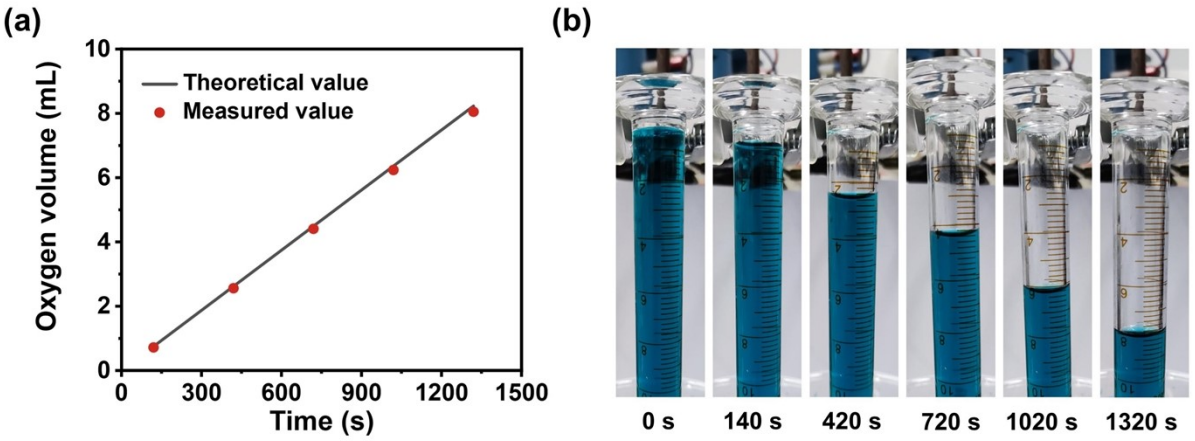

Figure S14 (a) Experimental and theoretical amounts of O_2 generated by the $Ru_{0.1}$-NiFeOOH/PO_4^{3-} electrode. (b) Optical photos of the measuring cylinder that is used to collect the oxygen.

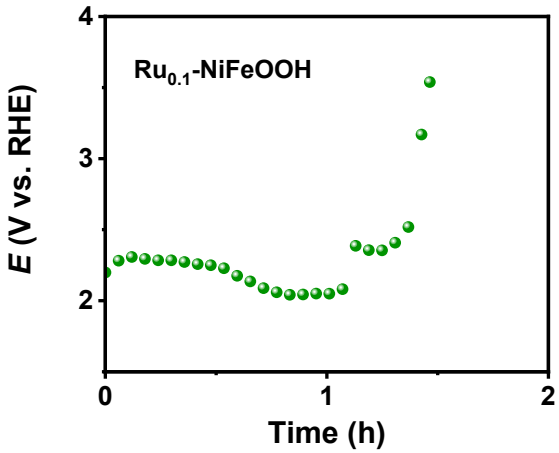

Figure S15 E-T curve of $Ru_{0.1}$-NiFeOOH in 6 M KOH + seawater at 0.5 A cm^{-2}.

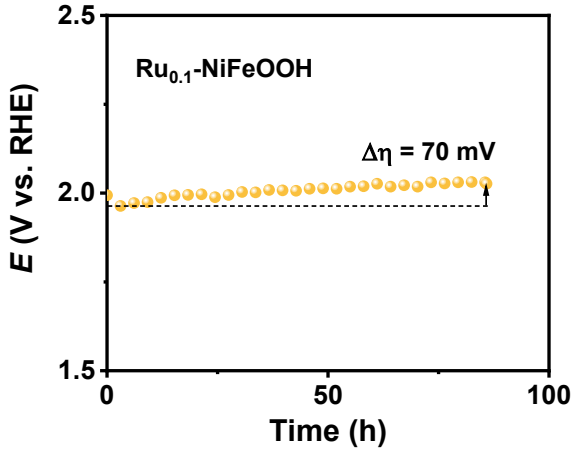

Figure S16 E-T curve of $Ru_{0.1}$-NiFeOOH in 1 M KOH + 2 M NaCl electrolyte at 0.5 A cm^{-2}.

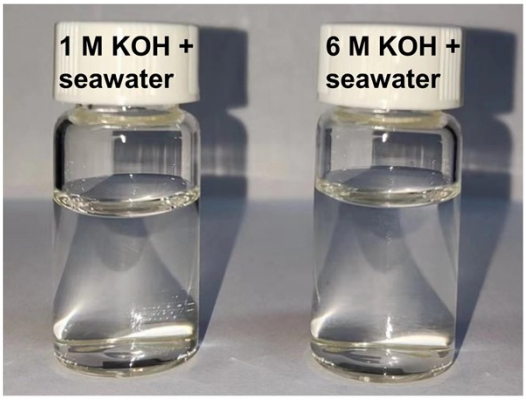

Figure S17 Optical images of detection results for ClO^- in 1 M KOH + seawater and 6 M KOH + seawater after 1,000 h stability test at 0.5 A cm^{-2}, respectively.

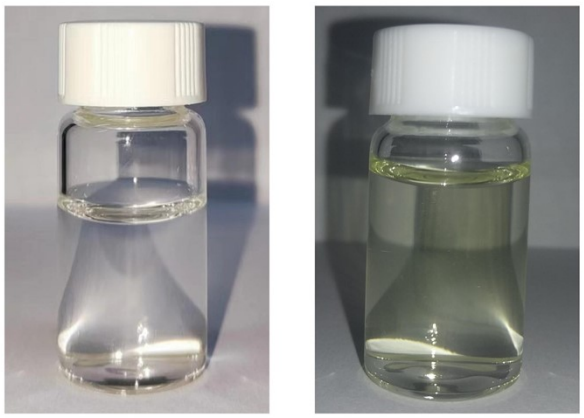

Figure S18 Optical images of detection results for ClO^- in 1 M KOH + 2 M NaCl after stability test at 0.5 A cm^{-2}.

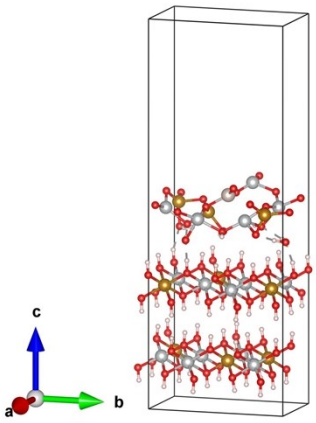

Figure S19 The main view of the $Ru_{0.1}$-NiFeOOH framework.

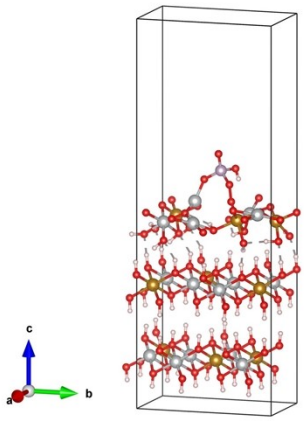

Figure S20 The main view of the NiFeOOH/PO_4^{3-} framework.

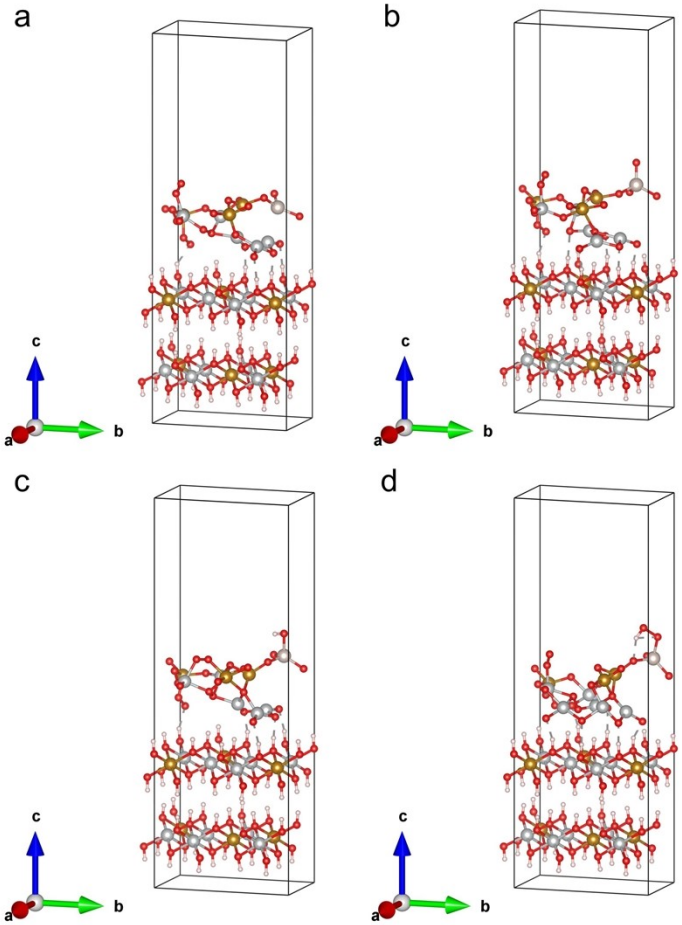

Figure S21 (a) The main view of the $Ru_{0.1}$-NiFeOOH/PO_4^{3-} framework and (b-d) the binding configurations of O*, OH*, and OOH* bonds on $Ru_{0.1}$-NiFeOOH/PO_4^{3-}.

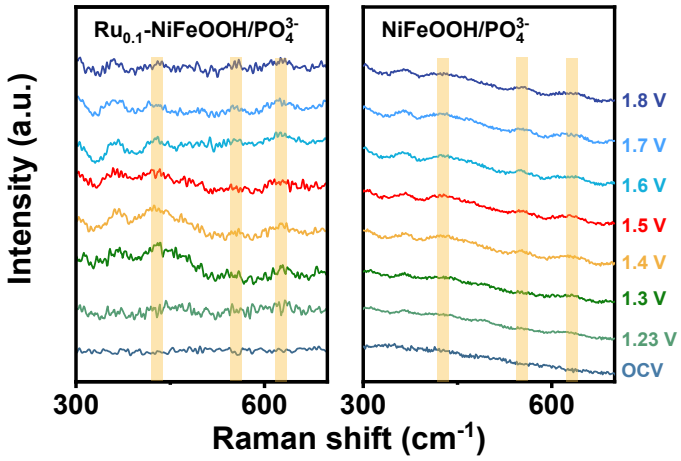

Figure S22 In-situ Raman spectra of $Ru_{0.1}$-NiFeOOH/PO_4^{3-} and NiFeOOH/PO_4^{3-}.

Figure S23 A picture displaying a commercial silicon solar cell-powered $Ru_{0.1}$-NiFeOOH/PO_4^{3-}||$Ru_{0.1}$-NiFeOOH/PO_4^{3-} seawater electrolysis with 1 cm^2 electrodes operating at 1,020 mA cm^{-2} under 2.2 V (25 ℃).

Table S1 The Ni, Fe, and Ru atomic occupancies in $Ru_{0.1}$-NiFeOOH/PO_4^{3-}.

Catalyst	Ni content (at %)	Fe content (at %)	Ru content (at %)
$Ru_{0.1}$-NiFeOOH/PO_4^{3-}	33.85	18.18	0.91

Table S2 The overpotentials of $Ru_{0.1}$-NiFeOOH/PO_4^{3-} at 10, 100, and 300 mA cm^{-2} in different electrolytes at 25 ℃.

Current density (mA cm^{-2})	1 M KOH (mV)	1 M KOH + 0.5 M NaCl (mV)	1 M KOH + Seawater (mV)
10	245	246	255
100	291	289	325
300	318	313	359

Table S3 Fitting EIS data of $Ru_{0.1}$-NiFeOOH/PO_4^{3-}, NiFeOOH/PO_4^{3-}, $Ru_{0.1}$-NiFeOOH, and RuO_2 at 25 ℃.

Catalyst	R_s (Ω)	R_{ct} (Ω)
$Ru_{0.1}$-NiFeOOH/PO_4^{3-}	1.54	14.73
NiFeOOH/PO_4^{3-}	1.34	39.37
$Ru_{0.1}$-NiFeOOH	1.22	83.21
RuO_2	1.40	72.25

Table S4 Overpotential comparison of seawater separation and similar seawater conditions for seawater separation of reported catalysts and $Ru_{0.1}$-$NiFeOOH/PO_4^{3-}$ in this work at different given current densities (containing 10, 100, and 300 mA cm^{-2}).

Catalyst	Current density (mA cm^{-2})	Overpotential (mV)	Ref.
$Ru_{0.1}$-$NiFeOOH/PO_4^{3-}$	10	255	This work
	100	325	
	300	359	
$Co_{3-x}Pd_xO_4$	10	370	[2]
$Fe_{0.05}$ CoNi LDH/NF	10	287	[3]
ER-P/RP-SNCF-5	10	346	[4]
Cr-Co_xP	100	325	[5]
NCFPO/C	100	370	[6]
NiFeLDH	300	370	[7]
NiFe/NiS_x-Ni	400	300	[8]

Table S5 The performance of seawater electrolysis driven by commercial silicon-based solar panels compared to reported literature.

Catalyst	Current (mA)	Voltage (V)	Ref.
$Ru_{0.1}$-NiFeOOH/PO_4^{3-}	1040	1.6	This work
	1020	2.2	-
$Ir_1/Ni_{1.6}Mn_{1.4}O_4$	1040	2.85	[9]
NiFe/NiS_x-Ni	876	2.75	[8]
Fe-Ni_2P_v	150	2.11	[10]
Co_xP_v@NC	49.3	1.792	[11]

Table S6 A comparison of the AEM seawater electrolyzer performance between $Ru_{0.1}$-$NiFeOOH/PO_4^{3-}$ and three reported electrocatalysts.

Catalyst	Fe,P-$NiSe_2$	NiFe LDH	Cr_2O_3-CoO_x	$Ru_{0.1}$-$NiFeOOH/PO_4^{3-}$
Cell efficiency at 500 mA cm^{-2} (%)	73.8	74.7	70.9	75.1
Current density at 1.8 V (mA cm^{-2})	800	250	700	1000
Highest current density (mA cm^{-2})	1144	1000	1000	2500
Faraday efficiency (%)	92	94	92	100
Durability (h)	200	2	100	100
Ref.	*Adv. Mater.* **2021**, *33*, 2101425.	*Energy Environ. Sci.* **2020**, *13*, 1725.	*Nat. Energy* **2023**, *8*, 264.	This work

Electrolyzer efficiency

H_2 production rate @ 0.5 A cm^{-2}

= (j A cm^{-2})(1 e^-/1.602 × 10^{-19} C)(1 H_2/2 e^-)

= 0.5 A cm^{-2} / (1.602 × 10^{-19} C x 2)

= 2.59 × 10^{-6} mol H_2 cm^{-2} s^{-1}

LHV of H_2

= 120 kJ g^{-1} H_2 = 2.42 × 105 J mol^{-1} H_2

H_2 power out

= (2.59 × 10^{-6} mol cm^{-2} s^{-1}) × (2.42 × 105 J mol^{-1})

= 0.627 W cm^{-2}

Electrolyzer Power of $Ru_{0.1}$-NiFeOOH/PO_4^{3-}||Pt/C

Electrolyzer Power ($Ru_{0.1}$-NiFeOOH/PO_4^{3-}) @ 0.5 A cm^{-2}

= (0.5 A cm^{-2}) (1.67 V)

= 0.835 W cm^{-2}

Efficiency of $Ru_{0.1}$-NiFeOOH/PO_4^{3-}||Pt/C

= (H_2 Power Out) / (Electrolyzer Power)

= 0.627 W cm^{-2}/0.835 W cm^{-2}

= 75.1%

References

1. X. Kang, F. Yang, Z. Zhang, H. Liu, S. Ge, S. Hu, S. Li, Y. Luo, Q. Yu, Z. Liu, Q. Wang, W. Ren, C. Sun, H.-M. Cheng, B. Liu, *Nat. Commun.* 2023, **14**, 3607.
2. N. Wang, P. Ou, S. F. Hung, J. E. Huang, A. Ozden, J. Abed, I. Grigioni, C. Chen, R. K. Miao, Y. Yan, J. Zhang, Z. Wang, R. Dorakhan, A. Badreldin, A. Abdel-Wahab, D. Sinton, Y. Liu, H. Liang, E. H. Sargent, *Adv. Mater.* 2023, **35**, 2210057.
3. A. Gupta, H. K. Sadhanala, A. Gedanken, *Electrochim. Acta* 2023, **470**, 143269.
4. F. Liu, R. Hu, H. Qiu, H. Miao, Q. Wang, J. Yuan, *J. Alloys Compd.* 2022, **913**, 165342.
5. Y. Song, M. Sun, S. Zhang, X. Zhang, P. Yi, J. Liu, B. Huang, M. Huang, L. Zhang, *Adv. Funct. Mater.* 2023, **33**, 2214081.
6. H. J. Song, H. Yoon, B. Ju, D. Y. Lee, D. W. Kim, *ACS Catal.* 2019, **10**, 702.
7. S. Dresp, F. Dionigi, S. Loos, J. Ferreira de Araujo, C. Spöri, M. Gliech, H. Dau, P. Strasser, *Adv. Energy Mater.* 2018, **8**, 1800338.
8. Y. Kuang, M. J. Kenney, Y. Meng, W. H. Hung, Y. Liu, J. E. Huang, R. Prasanna, P. Li, Y. Li, L. Wang, M, C. Lin, M. D. McGehee, X. Sun, H. Dai, *Proc. Natl. Acad. Sci.* 2019, **116**, 6624.
9. N. Wen, Y. Xia, H. Wang, D. Zhang, H. Wang, X. Wang, X. Jiao, D. Chen, *Adv. Sci.* 2022, **9**, 2200529.
10. X. Liu, Q. Yu, X. Qu, X. Wang, J. Chi, L. Wang, *Adv. Mater.* 2023, **36**, 2307395.
11. X. Wang, X. Liu, S. Wu, K. Liu, X. Meng, B. Li, J. Lai, L. Wang, S. Feng, *Nano Energy* 2023, **109**, 108292.